

COMPARATIVE STUDY OF FAST FOCUS MODE AND SLOW FOCUS MODE  
IN PLASMA FOCUS DEVICES

VAHID DAMIDEH

Centre for Plasma Research  
INTI International University  
2016

COMPARATIVE STUDY OF FAST FOCUS MODE AND SLOW FOCUS MODE  
IN PLASMA FOCUS DEVICES

by

VAHID DAMIDEH

being a thesis submitted to  
INTI International University  
in candidature for the degree of  
Doctor of Philosophy

Centre for Plasma Research  
INTI International University  
2016



**INTI**  
International University  
LAUREATE INTERNATIONAL UNIVERSITY

## POSTGRADUATE PROGRAMME CERTIFICATION OF DOCTORAL THESIS

Author's Full Name : Vahid Damideh

Student I.D : 113003955

Thesis Title : Comparative Study of Fast Focus Mode and Slow Focus Mode in Plasma Focus Devices

Academic Session : July 2013 – June 2016

With regard to Clause 4.2 of the INTI Student Intellectual Property Policy (Supplementary), the thesis is the student's property. Thereby declare this thesis as:

CONFIDENTIAL

☐

Consisting of classified information under the OFFICIAL SECRETS ACT 1972

RESTRICTED

☐

Consisting of RESTRICTED information which has been determined by the organisation/body where the research was conducted.

OPEN ACCESS/NON-RESTRICTED

☒

I allow this thesis to be published through open access, full text or copied for study, learning and research purposes only.

For the Open Access/Non-Restricted category, I allow this (Master's/Doctoral) thesis to be kept in the INTI International University (INTI) Library with the following usage conditions:

1. INTI Library has the right to reproduce the thesis for study, learning and research purposes only.
2. INTI Library is allowed to make one (1) copy of this thesis for exchange purpose among higher education institutions and any government body/agency, subject to terms and conditions.

STUDENT SIGNATURE

VERIFIED BY:

SUPERVISOR'S  
SIGNATURE

Y21178650

(IDENTITY CARD/PASSPORT  
NO.)

Date : 10/3/2016

Professor Dr. Saw Sor Heoh

SUPERVISOR'S NAME

Date: 10/3/2016

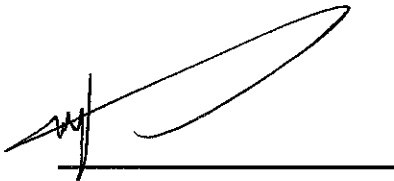
## **COPYRIGHT**

The copyright of this thesis belongs to the author under the terms of the Copyright Act 1987 as qualified by Section 4 of INTI International University Intellectual Property Policy. Due acknowledgement shall always be made of the use of any material contained in, or derived from, this thesis.

© Vahid Damideh, 2016  
All Rights reserved

## DECLARATION

I hereby declare that the work has been done by myself and no portion of the work contained in this thesis has been submitted in support of any application for any other degree or qualification of this or any other university or institute of learning.

A handwritten signature in black ink, consisting of a stylized 'V' followed by a long, sweeping horizontal stroke that curves upwards at the end.

Vahid Damideh

## ACKNOWLEDGEMENTS

By giving glory to Great Allah who has given all His provisions and sustenance in the completion of this piece of work, I am sincerely thankful to Prof. Dr. Asghar Sadighzadeh who was the first one trusted, encouraged and supported me.

I am deeply appreciating the supervision of Prof. Dr. Saw Sor Heoh and Prof. Dr. Lee Sing. They are great, high-minded and high-hearted scientists who guided and supported me in my study and even in my life in Malaysia. I have learnt a lot from them.

In addition, I am also grateful to the Centre for Plasma Research for the laboratory facilities and Nanyang Technological University Singapore for the gift of 3kJ Plasma Focus Machine and 160 kJ DuPF Capacitor bank to INTI IU.

Lastly, I am blessed with the support of my lovely family. Their words of encouragements and love gave me the drive to go through this study.

## Abstract

In this thesis comparison between Fast Focus Mode (FFM) and Slow Focus Mode (SFM) in plasma focus devices is studied. For INTI PF machine, results of numerical experiments based on Lee Model Code on Deuterium, Neon and Argon in the pressure range of 1 Torr to 14 Torr D, 1 Torr to 5.5 Torr Ne and 0.2 Torr to 2.4 Torr Ar show that as a rule-of-thumb, diameter-optimized SFM is considered to occur when fast plasma stream speed generated by pinch column is equal to the peak axial phase speed. Results of speed factor, FIB energy, FPS energy, FIB damage factor, plasma footprint radius for FFM and SFM at different pressures of D, Ne and Ar are presented. These results may be used to predict different applications of both modes: especially in the fields of nuclear fusion reactor first wall materials and its related investigations by time-matched FFM; and thin film nano-material synthesis by diameter-optimized SFM. Design and construction of a PMT-Scintillator diagnostic system for D-D fusion Neutron time-of-flight measurements (TOF) in INTI PF machine are presented. In addition, a fast 50  $\Omega$  Faraday Cup was designed and fabricated to enable time-of-flight TOF measurements of pulsed ion beam of INTI PF. The shortest FWHM for ion pulse captured by Faraday Cup was 27 ns. In this research the correlation of the ion beam energy between TOF measurements and Lee Model Code with different kind of filling gases such as D, Ne, Ar, Kr and Xe is presented. The results show there is acceptable correlation between TOF measurements and Lee Model Code. The maximum most common energy for D, Ne, Ar, Kr and Xenon ions generated by pinch column, detected by Faraday Cup were 67 keV, 485 keV, 1.2 MeV, 3.9 MeV and 6 MeV consistent with the values predicted by Lee Model Code. In the cases of Ar, Kr and Xe, Radiative Collapse effect leads to very small pinch radius size which is calculated by Lee Model Code. In order to study the application of INTI plasma focus machine in the field of advanced material sciences, some experiments such as graphite deposition on silicon wafer, hardening by nitriding and also fusion first wall material research by using tungsten targets are presented. Conceptual design of 160 kJ DuPF as a biggest plasma focus facility in the world for material research, by using Lee Model code in both FFM and SFM at different pressures of different kind of filling gases such as D, Ne and Ar is presented. It seems that reliable SFM for all gases occur when the ratio of FPS speed to axial velocity is near to 1. Finally, industrial detail design of DuPF and its parts by using SolidWorks software is presented.

## Table of Contents

|  |     |
|--|-----|
| COPYRIGHT  | ii  |
| DECLARATION  | iii |
| ACKNOWLEDGMENTS  | iv  |
| Abstract   | v   |
| Table of Contents  | vi  |
| List of Tables   | ix  |
| List of Figures  | xi  |
| CHAPTER 1 Introduction and Literature Review                           | 1   |
| 1.1 Problem Statement  | 4   |
| 1.2 Research Objectives  | 4   |
| 1.3 Continuation of the Literature Review                              | 5   |
| 1.3.1 Nano-materials   | 5   |
| 1.3.2 Fusion first wall materials                                      | 8   |
| 1.3.3 Slow Focus Mode (SFM)  | 12  |
| 1.4 Thesis Outline   | 15  |
| CHAPTER 2 Plasma Focus Characteristics                                 | 17  |
| 2.1 Plasma Focus Simulation  | 17  |
| 2.2 The Lee Model Code   | 20  |
| 2.3 Description of the Lee Code  | 20  |
| 2.4 Procedure for Using the Code                                       | 24  |
| CHAPTER 3  | 26  |
| Numerical study of FFM and SFM of INTI PF machine using Lee Model Code | 26  |
| 3.1 INTI PF Machine  | 26  |
| 3.2 Numerical experiments on INTI PF using Lee Model Code              | 26  |
| 3.2.1 Numerical experiments for operation in Deuterium                 | 27  |
| 3.2.2 Operation in Neon and Argon                                      | 40  |
| CHAPTER 4 Experimental Set up  | 52  |
| 4.1 INTI PF System   | 52  |
| 4.2 Diagnostics  | 53  |
| 4.3 Faraday Cup  | 55  |



|           |  |     |
|-----------|--|-----|
| 4.3.1     | Deuterium TOF measurements                                 | 71  |
| 4.3.2     | Neon TOF measurements                                      | 79  |
| 4.3.3     | Argon TOF measurements                                     | 85  |
| 4.3.4     | Krypton TOF measurements                                   | 91  |
| 4.3.5     | Xenon TOF measurements                                     | 110 |
| 4.4       | Photomultiplier-Scintillator System for INTI-PF machine    | 118 |
| 4.5       | Set-up for damage studies and results                      | 134 |
| 4.5.1     | Characterization of samples in damage studies              | 141 |
| 4.6       | Experimental set up for deposition experiments and results | 146 |
| 4.6.1     | Results and discussion for the deposition experiments      | 152 |
| 4.6.1.1   | Weight   | 152 |
| 4.6.1.2   | Thickness  | 154 |
| 4.6.1.3   | Chemical Composition                                       | 156 |
| 4.6.1.4   | Surface Morphology   | 161 |
| 4.6.1.5   | Summary for Deposition Experiments                         | 172 |
| 4.6.1.6   | Recommendations  | 172 |
| 4.7       | Nitriding by using INTI PF in FFM                          | 173 |
| 4.7.1     | Sample 1, S1 (10 Shots)                                    | 178 |
| 4.7.2     | Sample 2, S2 (30 Shots)                                    | 185 |
| 4.7.3     | Vickers Micro Hardness Result                              | 191 |
| CHAPTER 5 | Numerical experiments on 160 kJ DuPF                       | 193 |
| 5.1       | FFM operation of DuPF                                      | 196 |
| 5.1.1     | DuPF FFM operation using Deuterium                         | 197 |
| 5.1.2     | DuPF FFM operation using Neon                              | 199 |
| 5.1.3     | DuPF FFM operation using Argon                             | 200 |
| 5.2       | SFM operation of DuPF                                      | 201 |
| 5.2.1     | DuPF SFM operation using Deuterium                         | 201 |
| 5.2.2     | DuPF SFM operation using Neon                              | 202 |
| 5.2.3     | DuPF SFM operation using Argon                             | 204 |
| 5.3       | Comparative study of FFM and SFM in DuPF                   | 205 |
| CHAPTER 6 | Industrial detail design of 160 kJ DuPF                    | 225 |

|                      |                    |     |
|----------------------|--------------------|-----|
| 6.1                  | DuPF Electrodes    | 226 |
| 6.1.1                | FFM Electrodes     | 226 |
| 6.1.2                | SFM Electrodes     | 228 |
| 6.1.3                | Electrode Parts    | 230 |
| 6.2                  | DuPF Vacuum Vessel | 254 |
| 6.3                  | DuPF Main Table    | 267 |
| 6.4                  | DuPF Gas Panel     | 273 |
| 6.5                  | DuPF Spark Gaps    | 283 |
| 6.6                  | DuPF Sample Holder | 291 |
| CHAPTER 7 Conclusion |                    | 298 |
| References           |                    | 304 |

## List of Tables

|  |     |
|--|-----|
| Table 1.1 Typical ZaP Flow Z-Pinch operating parameters [23]   | 14  |
| Table 3.1 Results of numerical experiments based on Lee Model Code on INTI PF operated with Deuterium at different pressures.  | 29  |
| Table 3.2 Computed FFM and SFM results for 3 Torr and 14 Torr Deuterium based on Lee code in INTI PF   | 34  |
| Table 3.3 Results of numerical experiments based on Lee Model Code on INTI PF with Neon filling gas at different pressures.  | 41  |
| Table 3.4 Results of numerical experiments based on Lee Model Code on INTI PF with Argon filling gas at different pressures.   | 44  |
| Table 4.1 Physical Parameters needed for FC design   | 58  |
| Table 4.2 Lee Model parameters for different pressures of Deuterium by matching the computed to measured current traces  | 64  |
| Table 4.3 Summary of Numerical Experiment results generated by FIB Lee Model Code for INTI PF, 12kV, 2-12 Torr Deuterium. Model parameters of each pressure are fitted from measured current traces. | 64  |
| Table 4.4 Summary of Experimental results generated by fast Faraday Cup in INTI PF, 12kV, 2-12 Torr Deuterium.   | 67  |
| Table 4.5 Deuterium time of flight measurements in INTI PF machine   | 72  |
| Table 4.6 Neon Time of Flight measurements in correlation with Lee Model Code  | 80  |
| Table 4.7 Summary of Argon TOF measurements in INTI PF machine   | 86  |
| Table 4.8 Summary of Krypton ions time of flight measurements at 0.5 Torr, 12 kV in INTI PF machine  | 93  |
| Table 4.9 Summary of Xenon TOF measurements in correlation between Lee Model Code at 12 kV in INTI PF machine  | 110 |
| Table 4.10 Plastic and Liquid Scintillators Specifications for Neutron detection [111].  | 123 |
| Table 4.11 Voltage divider distribution for 9813QB PMT   | 128 |
| Table 4.12 Tungsten target samples: experimental set-up  | 137 |
| Table 4.13 Model and Operational parameters of shot for target sample 1  | 139 |
| Table 4.14 FIB and FPS data per shot simulated by Lee Code for selected shots of each sample.  | 139 |

|   |     |
|---|-----|
| Table 4.15 Parameters for Deposition Experiment using Neon  | 148 |
| Table 4.16 Specifications of TM3000 SEM   | 151 |
| Table 4.17 Specifications of EDX SwiftED3000  | 152 |
| Table 4.18 Mass of Thin Film Deposited  | 152 |
| Table 4.19 Chemical Composition at Center of S1, S2, S3, S4, S5 and S6 with 1.5 k Magnification   | 156 |
| Table 4.20 Chemical Composition at Area Above Center of S1, S2, S3, S4, S5 and S6 with 3.0 k Magnification  | 156 |
| Table 4.21 Chemical Composition at Center of SG5, SG8 and SG9 with 1.5 k Magnification  | 157 |
| Table 4.22 Chemical Composition at Area Above Center of SG5, SG8 and SG9 with 3.0 k Magnification   | 157 |
| Table 5.1 Tube, Model and Operation parameters of DuPF for D, Ne and Ar in FFM state.   | 197 |
| Table 5.2 Results of numerical experiments based on Lee Model Code on 160 kJ DuPF operated with Deuterium at different pressures during FFM operation | 198 |
| Table 5.3 Results of numerical experiments based on Lee Model Code on 160 kJ DuPF operated with Ne at different pressures during FFM operation.       | 199 |
| Table 5.4 Results of numerical experiments based on Lee Model Code on 160 kJ DuPF operated with Ar at different pressures during FFM operation.       | 200 |
| Table 5.5 Tube, Model and operational parameters of DuPF for SFM operation of Deuteium, Neon and Argon.   | 201 |
| Table 5.6 Results of numerical experiments based on Lee Model Code on 160 kJ DuPF operated with Deuterium at different pressures during SFM operation | 202 |
| Table 5.7 Results of numerical experiments based on Lee Model Code on 160 kJ DuPF operated with Ne at different pressures during SFM operation.       | 203 |
| Table 5.8 Results of numerical experiments based on Lee Model Code on 160 kJ DuPF operated with Ar at different pressures during SFM operation.       | 204 |
| Table 5.9 Comparative table of SFM and FFM for 160 kJ DuPF operated with Deuterium, Ne and Ar based on Lee Model Code                                 | 206 |

## List of Figures

|  |    |
|--|----|
| Figure 2.1 Schematic of the axial and radial phases. The left section depicts the axial phase, the right section the radial phase. In the left section, $z$ is the effective position of the current sheath-shock front structure. In the right section $r_s$ is the position of the inward moving shock front driven by the piston at position $r_p$ . Between $r_s$ and $r_p$ is the radially imploding slug, elongating with a length $z_f$ . The capacitor, static inductance and switch powering the plasma focus is shown for the axial phase schematic only [60]. | 22 |
| Figure 2.2 Schematic of radius versus time trajectories to illustrate the radial inward shock phase when $r_s$ moves radially inwards, the reflected shock (RS) phase when the reflected shock moves radially outwards, until it hits the incoming piston $r_p$ leading to the start of the pinch phase ( $t_f$ ) and finally the expanded column phase [60].  | 22 |
| Figure 3.1 Speed Factor versus Deuterium pressure in INTI PF based on Lee Model Code   | 30 |
| Figure 3.2 Fast ion energy versus deuterium pressure in INTI PF based on Lee Model Code  | 30 |
| Figure 3.3 FIB damage factor in INTI PF versus Deuterium pressure based on Lee Model Code  | 32 |
| Figure 3.4 Number of ions per shot in INTI PF versus Deuterium pressure based on Lee Model Code  | 32 |
| Figure 3.5 Ion current generated by INTI PF pinch column versus Deuterium pressure   | 33 |
| Figure 3.6 Number of neutrons per shot in INTI PF versus Deuterium pressure based on Lee Model Code  | 33 |
| Figure 3.7 Computed discharge current of INTI PF versus time based on Lee Model Code at 3 Torr Deuterium, FFM (left) and 14 Torr, SFM (right)  | 34 |
| Figure 3.8 Computed radial trajectories of INTI PF based on Lee Model Code for 3 Torr (left) and 14 Torr (right) Deuterium; FFM (left), SFM (right)  | 35 |
| Figure 3.9 Plasma footprint radius versus Deuterium pressure in INTI PF  | 36 |
| Figure 3.10 FPS energy per ion versus Deuterium pressure in INTI PF  | 37 |
| Figure 3.11 Plasma Stream energy versus pressure for Deuterium in INTI PF  | 37 |

|  |    |
|--|----|
| Figure 3.12 The ratio of plasma stream energy to FIB beam energy versus Deuterium pressure in INTI PF  | 38 |
| Figure 3.13 Computed discharge current of INTI PF versus time based on Lee Model Code at 2 torr Neon, FFM (left) and 5.5 torr, SFM (right)           | 40 |
| Figure 3.14 Computed radial trajectories of INTI PF based on Lee Model Code for 2 Torr (left) and 5.5 Torr (right) Neon; FFM (left), SFM (right)     | 42 |
| Figure 3.15 Computed discharge current of INTI PF versus time based on Lee Model Code at 0.4 Torr Argon, FFM (left) and 2.5 Torr Ar, SFM (right)     | 43 |
| Figure 3.16 Computed radial trajectories of INTI PF based on Lee Model Code for 3 Torr (left) and 14 Torr (right) Deuterium; FFM (left), SFM (right) | 43 |
| Figure 3.17 Speed Factor versus Neon and Argon pressure in INTI PF based on Lee Model Code   | 45 |
| Figure 3.18 Fast ion beam energy (per ion) versus Neon and Argon pressure in INTI PF based on Lee Model Code   | 45 |
| Figure 3.19 FIB damage factor for Neon and Argon versus pressure in INTI PF based on Lee Model Code  | 46 |
| Figure 3.20 computed number of ions per shot in INTI PF based on Lee Model Code for Neon and Argon versus pressure                                   | 47 |
| Figure 3.21 Plasma footprint radius generated from pinch column versus Ne and Ar pressure in INTI PF   | 47 |
| Figure 3.22 Ion current generated by pinch column versus Ne and Ar pressure in INTI PF   | 48 |
| Figure 3.23 FPS energy per ion versus Ne and Ar pressure in INTI PF  | 48 |
| Figure 3.24 FPS energy %E0 versus Neon and Argon pressure in INTI PF   | 49 |
| Figure 3.25 The ratio of plasma stream energy to FIB energy versus Ne and Ar pressure in INTI PF   | 50 |
| Figure 4.1 Schematic diagram of INTI PF machine, Center for Plasma Research, INTI International University   | 53 |
| Figure 4.2 SXR measurement in INTI PF Machine  | 55 |
| Figure 4.3 Biasing circuit for INTI-PF Faraday Cup   | 59 |
| Figure 4.4 Assembled INTI-PF Faraday Cup   | 60 |
| Figure 4.5 Deuteron's energy versus time of flight during 4cm flight length  | 62 |

|  |    |
|--|----|
| Figure 4.6 Axial peak velocity, Speed factor and Ion current expected from FC with variation of Deuterium pressure in INTI PF, based on Lee Code. The model parameters $f_m$ , $f_c$ , $f_{mr}$ , $f_{cr}$ for each shot are fitted by matching the computed current trace to the measured current trace of that shot.                                   | 63 |
| Figure 4.7 Experimental current fitted by Lee Code including XR, FC and Voltage probe signals, 12kV, Deuterium, INTI PF, Fast Focus Mode (3 Torr and 37 ns FWHM, left side) and Slow Focus Mode (12 Torr and $> 2\mu s$ FWHM, right side). The fitted model parameters ( $f_m$ , $f_c$ , $f_{mr}$ , $f_{cr}$ ) of the FFM shot are: 0.07, 0.7, 0.2, 0.7. | 65 |
| Figure 4.8 $dN/dE$ and Number of Ions versus energy achieved by Faraday Cup signals for INTI PF at FFM (right) and SFM (left) operations.  | 66 |
| Figure 4.9 Numerical experiments based on Lee Code show that plasma footprint area of SFM (right, 12 Torr) is at least 10 times more than its FFM (left, 3 Torr) in INTI PF  | 67 |
| Figure 4.10 Ion Flux correlation between Lee Code (red trace, RHS scale) and Faraday Cup (blue trace, LHS scale)   | 68 |
| Figure 4.11 Number of fast ions (1keV) from Faraday Cup and Damage Factor from Lee Model Code  | 69 |
| Figure 4.12 Slow Ions Number ratio to Fast Ions Number and FWHM measured by Faraday Cup in different pressures of Deuterium at 12 kV discharge voltage in INTI PF.   | 70 |
| Figure 4.13 Mean Ion energy measured by FC and FPS energy per ion calculated by Lee Model Code, decreasing by increasing of Deuterium pressure   | 70 |
| Figure 4.14 Current fitting of Test 446, 3 Torr, D, 12 kV  | 73 |
| Figure 4.15 FC and TOF signal for Test 446, 3 Torr, D, 12 kV in INTI PF machine  | 73 |
| Figure 4.16 Radial trajectories for Test 446, 3 Torr D, 12 kV, predicted by Lee Model Code during proper current fitting   | 74 |
| Figure 4.17 Current fitting of test 445, 3 Torr, D at 12 kV in INTI PF machine   | 74 |
| Figure 4.18 FC and TOF signal for test 445, 3 Torr, D, 12 kV in INTI PF machine  | 75 |
| Figure 4.19 Radial trajectories for Test 445, 3 Torr D, 12 kV, predicted by Lee Model Code during proper current fitting   | 75 |

|  |    |
|--|----|
| Figure 4.20 Current fitting for test 416, 8 Torr, D at 12 kV using Lee Model Code                                      | 76 |
| Figure 4.21 FC TOF signal for test 416, 8 Torr, D at 12 kV in INTI PF machine  | 76 |
| Figure 4.22 Radial trajectories of test 416, 8 Torr, D at 12 kV during proper current fitting                          | 77 |
| Figure 4.23 Deuterium Ion energy versus pressure from FC and Lee Model Code  | 77 |
| Figure 4.24 Current fitting of test 883, 3 Torr, Ne at 12 kV in INTI PF machine  | 81 |
| Figure 4.25 Faraday Cup and TOF signal for test 883, 3 Torr, Ne at 12 kV   | 82 |
| Figure 4.26 Radial trajectories for test 883, 3 Torr, Ne at 12 kV, predicted by Lee Model Code during proper fitting   | 82 |
| Figure 4.27 Faraday Cup and TOF signal for test 872, 2 Torr, Ne at 12 kV   | 83 |
| Figure 4.28 Current fitting of test 872, 2 Torr, Ne at 12 kV in INTI PF machine  | 83 |
| Figure 4.29 Radial trajectories for test 872, 2 Torr, Ne at 12 kV, predicted by Lee Model Code during proper fitting   | 84 |
| Figure 4.30 Correlation between Lee Model Code and FC TOF results for 2 Torr - 4 Torr Neon at 12 kV in INTI PF machine | 84 |
| Figure 4.31 TOF measurements of test 859, 0.9 Torr Srgon at 12 kV in INTI PF machine                                   | 87 |
| Figure 4.32 Current fitting of test 859, 0.9 Torr, Argon at 12 kV in INTI PF machine                                   | 88 |
| Figure 4.33 TOF measurements of test 859, 0.9 Torr Argon at 12 kV in INTI PF machine, 150 MHz bandwidth limit          | 88 |
| Figure 4.34 Radial trajectories of test 859, 0.9 Torr, Argon at 12 kV including radiative collapse in INTI PF machine  | 89 |
| Figure 4.35 Original TOF signal of test 852, 0.8 Torr Argon at 12 kV in INTI PF machine                                | 89 |
| Figure 4.36 Current fitting of test 852, 0.8 Torr, Argon at 12 kV in INTI PF machine                                   | 90 |
| Figure 4.37 Magnified FC TOF signal for test 852, 0.8 Torr Argon at 12 kV  | 90 |
| Figure 4.38 Correlation between Lee Model Code and FC TOF measurements results for Argon in INTI PF machine            | 91 |



|  |     |
|--|-----|
| Figure 4.39 Original TOF signal of test 897, 0.5 Torr, Krypton at 12 kV in INTI PF machine   | 94  |
| Figure 4.40 Current fitting of test 897, 0.5 Torr Krypton at 12 kV in INTI PF machine  | 95  |
| Figure 4.41 Magnified FC, Current, Voltage and pin-diode signals for test 897, 0.5 Torr Krypton at 12 kV in INTI PF machine  | 95  |
| Figure 4.42 Radial trajectories of test 897, 0.5 Torr Krypton at 12 kV in INTI PF machine; Radiative Collapse effect is clear at the end of radial piston trajectory in pink color | 96  |
| Figure 4.43 Original TOF signal of test 901, 0.5 Torr Krypton at 12 kV in INTI PF machine  | 97  |
| Figure 4.44 Current fitting of test 901, 0.5 Torr, Krypton at 12 kV in INTI PF machine   | 98  |
| Figure 4.45 Magnified FC, Current, Voltage and pin-diode signals of test 901, 0.5 Torr Krypton at 12 kV in INTI PF machine   | 98  |
| Figure 4.46 Radial trajectories of test 901, 0.5 Torr, Krypton at 12 kV in INTI PF machine calculated by Lee Model Code  | 99  |
| Figure 4.47 Original signal of test 902, 0.5 Torr, Krypton at 12 kV in INTI PF machine   | 100 |
| Figure 4.48 Current fitting of test 902, 0.5 Torr, Krypton at 12 kV in INTI PF machine   | 101 |
| Figure 4.49 Magnified FC, Current, Voltage and pin-diode signals of test 902, 0.5 Torr Krypton at 12 kV in INTI PF machine   | 101 |
| Figure 4.50 Computed radial trajectories of test 902, 0.5 Torr krypton at 12 kV in INTI PF machine including its radiative collapse effect at the end of radial phase              | 102 |
| Figure 4.51 Original signal of test 905, 0.5 Torr Krypton at 12 kV in INTI PF machine  | 103 |
| Figure 4.52 Current fitting of test 905, 0.5 Torr Krypton at 12 kV in INTI PF machine  | 104 |
| Figure 4.53 Magnified FC, Current, Voltage and pin-diode signals of test 905, 0.5 Torr Krypton at 12 kV  | 104 |
| Figure 4.54 Radial trajectories of test 905, 0.5 Torr Krypton at 12 kV in INTI PF machine including its radiative collapse effect at the end of radial phase                       | 105 |

|  |     |
|--|-----|
| Figure 4.55 Original signal of test 906, 0.5 Torr Krypton at 12 kV in INTI PF machine  | 106 |
| Figure 4.56 Current fitting of test 906, 0.5 Torr Krypton at 12 kV in INTI PF machine  | 107 |
| Figure 4.57 Magnified FC, Current, Voltage and pin-diode signals for test 906, 0.5 Torr Krypton at 12 kV   | 107 |
| Figure 4.58 Radial trajectories of test 906, 0.5 Torr Krypton at 12 kV in INTI PF machine including its radiative collapse effect at the end of radial phase | 108 |
| Figure 4.59 Correlation between Lee Model Code and FC TOF measurements results for 0.5 Torr Krypton at 12 kV for each of 10 shots in INTI PF machine         | 109 |
| Figure 4.60 Original signals of test 887, 0.33 Torr Xenon at 12 kV in INTI PF machine  | 111 |
| Figure 4.61 Current fitting of test 887, 0.33 Torr Xenon at 12 kV in INTI PF machine   | 112 |
| Figure 4.62 Magnified FC, Current, Voltage and pin-diode signals of test 887, 0.33 Torr Xenon at 12 kV in INTI PF machine                                    | 112 |
| Figure 4.63 Radial trajectories of test 887, 0.33 Torr Xenon at 12 kV in INTI PF machine including radiative collapse effect at the end of radial phase      | 113 |
| Figure 4.64 Original signals of test 894, 0.33 Torr Xenon at 12 kV in INTI PF machine  | 114 |
| Figure 4.65 Current fitting of test 894, 0.33 Torr Xenon at 12 kV in INTI PF machine   | 115 |
| Figure 4.66 Magnified FC, Current, Voltage and pin-diode signals of test 894, 0.33 Torr Xenon at 12 kV in INTI PF machine                                    | 115 |
| Figure 4.67 Radial trajectories of test 894, 0.33 Torr Xenon at 12 kV in INTI PF machine including its radiative collapse effect at the end of radial phase  | 116 |
| Figure 4.68 Correlation between Lee Model Code and FC TOF results for Xenon at 12 kV in INTI PF machine  | 117 |
| Figure 4.69 9813QB PMT tube  | 122 |
| Figure 4.70 A NE102A plastic scintillator  | 123 |
| Figure 4.71 NE102 scintillator coupling to PMT window by means of thin layer of clear silicone   | 124 |

|   |     |
|---|-----|
| Figure 4.72 9813QB PMT Voltage-divider circuit with consideration of pulse output linearity and to minimize ringing and high-voltage power supply noise is designed for INTI PF device. | 125 |
| Figure 4.73 Typical voltage gain characteristics for 9813QB PMT   | 128 |
| Figure 4.74 INTI PF PMT Voltage Divider   | 129 |
| Figure 4.75 INTI PMT up to $\pm 5$ kV, 2 mA Power Supply  | 130 |
| Figure 4.76 INTI PF PMT-Scintillator Galvanized iron housing  | 130 |
| Figure 4.77 12kV, 2.5 Torr Deuterium signals, $dI/dt$ (Yellow), PMT-Scintillator (Blue), Faraday Cup (Pink), XR pin-diode (Green).  | 132 |
| Figure 4.78 2.4541 MeV D-D neutron detecting from PMT-Scintillator detector in INTI PF, 12 kV, 2.5 Torr,  | 134 |
| Figure 4.79 Experimental set up, adjustable sample holder and shutter for INTI PF   | 136 |
| Figure 4.80 INTI plasma focus adjustable sample holder  | 136 |
| Figure 4.81 tungsten target samples 1, 2, 4 and 3 (right to left) after plasma focus firing   | 138 |
| Figure 4.82 INTI PF measured signals at 12kV, 2.5 Torr Deuterium accompanied by Lee Code fitting (shot 295- Sample 1)   | 138 |
| Figure 4.83 INTI PF measured signals at 12kV, 2.5 Torr Deuterium accompanied by Lee Code fitting (shot 300- Sample 2)   | 140 |
| Figure 4.84 INTI PF recorded signals at 12kV, 2.5 Torr Deuterium accompanied by Lee Code fitting (shot 310- Sample 3)   | 141 |
| Figure 4.85 INTI PF measured signals at 12kV, 2.5 Torr Deuterium accompanied by Lee Code fitting (shot 312- Sample 4)   | 141 |
| Figure 4.86 SEM image of tungsten target sample 1. Single shot without shutter. 12kV, 2.5 Torr, D.  | 142 |
| Figure 4.87 EDX analyzes for Tungsten target sample 1   | 142 |
| Figure 4.88 SEM image of tungsten target sample 2. 5 shots, 12kV, 2.5 Torr, D.  | 143 |
| Figure 4.89 XRD results for Tungsten target sample 2.   | 143 |
| Figure 4.90 SEM image of tungsten target sample 3 placed at 8 cm. Holes and cracks are much less than other samples. 10 shots, 12kV, 2.5 Torr, D.                                       | 144 |
| Figure 4.91 SEM image of tungsten target sample 4 placed at 6 cm from anode tip. Exposure is 10 shots, at 12kV, 2.5 Torr, D.  | 145 |

|  |     |
|--|-----|
| Figure 4.92 Graphite Target Fixed on Anode Tip   | 147 |
| Figure 4.93 Silicon Substrate Fixed on Sample holder   | 147 |
| Figure 4.94 Areas on Samples That Are to Be Analyzed   | 148 |
| Figure 4.95 Silicon Wafer (left), Silicon Substrates (right)   | 148 |
| Figure 4.96 Acetone, Iso-propanol, DI-water, Hotplate Stirrer (From left to right)                       | 149 |
| Figure 4.97 Hitachi TM3000 SEM Tabletop  | 150 |
| Figure 4.98 Graph of Mass of Thin Film Deposited (1 shot) on S1, S2, S3 and S4 as a function of pressure | 153 |
| Figure 4.99 Graph of Mass of Thin Film Deposited (5 shots) on S5 and S6 as a function of pressure        | 153 |
| Figure 4.100 Average Thickness of S1, S2, S3 and S4 over respective Gas Pressure                         | 155 |
| Figure 4.101 Average Thickness of S5 and S6 over respective Gas Pressure                                 | 155 |
| Figure 4.102 Average Thickness of SG5, SG8 and SG9 over respective Gas Pressure                          | 155 |
| Figure 4.103 Chemical Composition at Center of S1, S2, S3 and S4 over respective Gas Pressure            | 158 |
| Figure 4.104 Chemical Composition at Center of S5 and S6 over respective Gas Pressure                    | 159 |
| Figure 4.105 Chemical Composition at Area above Center of S1, S2, S3 and S4 over respective Gas Pressure | 159 |
| Figure 4.106 Chemical Composition at Area Above Center of S5 and S6 over respective Gas Pressure         | 160 |
| Figure 4.107 Chemical Composition at Center of SG5, SG8 and SG9 over respective Gas Pressure             | 160 |
| Figure 4.108 Chemical Composition at Area Above Center of SG5, SG8 and SG9 over respective Gas Pressure  | 160 |
| Figure 4.109 Center of S1  | 162 |
| Figure 4.110 Center of S2  | 162 |
| Figure 4.111 Center of S3  | 163 |
| Figure 4.112 Center of S4  | 163 |
| Figure 4.113 Area above Center of S1   | 164 |

|   |     |
|---|-----|
| Figure 4.114 Area above Center of S2                                  | 165 |
| Figure 4.115 Area above Center of S3                                  | 165 |
| Figure 4.116 Area above Center of S4                                  | 166 |
| Figure 4.117 Center of S5   | 167 |
| Figure 4.118 Center of S6   | 167 |
| Figure 4.119 Area above Center of S5                                  | 168 |
| Figure 4.120 Area above Center of S6                                  | 168 |
| Figure 4.121 Center of SG5  | 169 |
| Figure 4.122 Center of SG8  | 169 |
| Figure 4.123 Center of SG9  | 170 |
| Figure 4.124 Area above Center of SG5                                 | 170 |
| Figure 4.125 Area above Center of SG8                                 | 171 |
| Figure 4.126 Area above Center of SG9                                 | 171 |
| Figure 4.127 The surface of the Low Carbon Steel                      | 173 |
| Figure 4.128 Comparison of the Sample 0, Sample 1 and Sample 2        | 174 |
| Figure 4.129 Sample 0 which remains untreated                         | 174 |
| Figure 4.130 Sample 1 (a) Before Nitriding (b) After Nitriding        | 175 |
| Figure 4.131 Sample 2 (a) Before Nitriding (b) After Nitriding        | 175 |
| Figure 4.132 Sample 0 at the magnifications of X150 at the spot       | 176 |
| Figure 4.133 Sample 0 at the magnifications of x1000 at the spot      | 176 |
| Figure 4.134 Sample 0 at the magnifications of X150 at the periphery  | 177 |
| Figure 4.135 Sample 0 at the magnifications of X1000 at the periphery | 177 |
| Figure 4.136 Area Selection of the Sample 0 for EDX                   | 178 |
| Figure 4.137 EDX Elemental Analysis of the Sample 0                   | 178 |
| Figure 4.138 Sample 1 at the magnifications of X150 at spot           | 180 |
| Figure 4.139 Sample 1 at the magnifications of X500 at spot           | 181 |
| Figure 4.140 Sample 1 at the magnifications of X1000 at spot          | 181 |
| Figure 4.141 Sample 1 at the magnifications of x150 at periphery      | 182 |
| Figure 4.142 Sample 1 at the magnifications of x500 at periphery      | 182 |
| Figure 4.143 Sample 1 at the magnifications of x1000 at periphery     | 183 |

|  |     |
|--|-----|
| Figure 4.144 Cross Sectional View of Sample 1  | 184 |
| Figure 4.145 Magnified Cross Sectional View of Sample 1  | 184 |
| Figure 4.146 Area Selection of the Sample 1 for the EDX  | 185 |
| Figure 4.147 EDX Elemental Analysis of the Sample 1  | 185 |
| Figure 4.148 Sample 2 at the magnifications of X150 at spot  | 187 |
| Figure 4.149 Sample 2 at the magnifications of X500 at spot  | 187 |
| Figure 4.150 Sample 2 at the magnifications of X1000 at spot   | 188 |
| Figure 4.151 Sample 2 at the magnifications of x150 at periphery   | 188 |
| Figure 4.152 Sample 2 at the magnifications of x500 at periphery   | 189 |
| Figure 4.153 Sample at the magnifications of x1000 at periphery  | 189 |
| Figure 4.154 Cross Sectional View of Sample 2  | 190 |
| Figure 4.155 Magnified Cross Sectional View of Sample 2  | 190 |
| Figure 4.156 Area Selection of the Sample 2 for the EDX  | 191 |
| Figure 4.157 EDX Elemental Analysis of the Sample 2  | 191 |
| Figure 4.158 EDX Elemental Analysis of the Sample 2  | 192 |
| Figure 5.1 Outward appearance of the DPF devices; a- PF6 device; b- PF10 device; c- 3 kJ DPF device [65]   | 194 |
| Figure 5.2 Large DPF facilities; middle level of the three-floor PF-1000 installation [65]   | 194 |
| Figure 5.3 Vertical section of DPF chambers optimized for SXR production; MPS [65]   | 195 |
| Figure 5.4 Computed tube current and radial trajectories of 160 kJ DuPF based on Lee Model Code for 3 Torr (left) and 14 Torr (right) Deuterium; FFM (left), SFM (right)   | 208 |
| Figure 5.5 Computed tube current and radial trajectories of 160 kJ DuPF based on Lee Model Code for 2 Torr (left) and 2.7 Torr (right) Neon; FFM (left), SFM (right)   | 209 |
| Figure 5.6 Computed tube current and radial trajectories of 160 kJ DuPF based on Lee Model Code for 1 Torr (left) and 1.5 Torr (right) Argon; FFM (left), SFM (right); the radiative collapse compression in the case of 1 Torr Argon is considerable at the end of radial phase | 210 |
| Figure 5.7 Number of neutrons per shot for FFM and SFM at 160 kJ DuPF using Deuterium  | 211 |

|  |     |
|--|-----|
| Figure 5.8 Speed Factor versus pressure in DuPF for FFM and SFM using D, Ne and Ar.  | 212 |
| Figure 5.9 FIB damage factor of FFM and SFM of DuPF for D, Ne and Ar   | 214 |
| Figure 5.10 FPS Speed at the exit point versus pressure in DuPF using D, Ne and argon  | 215 |
| Figure 5.11 Plasma footprint radius at DuPF for its FFM and SFM operation using D, Ne and Ar   | 216 |
| Figure 5.12 Energy into plasma in % of $E_0$ versus Pressure for FFM and SFM configuration of DuPF using D, Ne and Ar                | 217 |
| Figure 5.13 Number of ions per shot for FFM (5cm anode radius ) and SFM (10 cm anode radius) operation of DuPF in D, Ne and Ar       | 219 |
| Figure 5.14 FIB Energy versus pressure in DuPF during FFM and FFM using D, Ne and Ar   | 220 |
| Figure 5.15 FPS energy to FIB energy ratio during FFM and SFM operations of DuPF using D, Ne and Ar                                  | 221 |
| Figure 5.16 FPS energy per ion in DuPF during FFM and SFM run using D, Ne and Ar   | 222 |
| Figure 5.17 Ratio of FPS speed to axial velocity in DuPF for FFM (5 cm anode radius) and SFM (10 cm anode radius) using D, Ne and Ar | 223 |
| Figure 6.1 DuPF-FFM electrodes   | 226 |
| Figure 6.2 Cross section view of DuPF-FFM electrodes   | 227 |
| Figure 6.3 2-D and 3-D drawings of DuPF-FFM electrodes   | 228 |
| Figure 6.4 DuPF-SFM electrodes   | 229 |
| Figure 6.5 Cross section view of DuPF-SFM electrodes   | 229 |
| Figure 6.6 2-D and 3-D views of DuPF-SFM   | 230 |
| Figure 6.7 Different parts of DuPF electrodes  | 231 |
| Figure 6.8 Main cathode base plate   | 233 |
| Figure 6.9 Cathode bars, 24 pieces for SFM and 12 pieces for FFM   | 234 |
| Figure 6.10 DuPF-SFM Cathode bars ring   | 235 |
| Figure 6.11 DuPF-SFM PTFE Insulator which insulates anode from cathode at the back of electrodes                                     | 236 |
| Figure 6.12 DuPF-SFM anode base plate  | 237 |
| Figure 6.13 DuPF-SFM Pyrex insulator   | 238 |

|  |     |
|--|-----|
| Figure 6.14 DuPF-SFM anode tube end disc   | 239 |
| Figure 6.15 DuPF-SFM anode tube, 20 cm diameter and 70 cm height   | 240 |
| Figure 6.16 DuPF-FFM minor cathode plate, additional component for FFM<br>which can be assembled on main cathode plate to change FFM<br>radius | 241 |
| Figure 6.17 DuPF-FFM cathode bars ring   | 242 |
| Figure 6.18 DuPF-FFM PTFE Insulator which insulate anode from cathode at<br>the back of electrodes   | 243 |
| Figure 6.19 DuPF-FFM anode base  | 244 |
| Figure 6.20 DuPF-FFM Pyrex insulator   | 245 |
| Figure 6.21 DuPF-FFM anode tube end-disc   | 246 |
| Figure 6.22 DuPF-FFM anode tube  | 247 |
| Figure 6.23 DuPF anode back glass  | 248 |
| Figure 6.24 DuPF anode high voltage disc   | 249 |
| Figure 6.25 DuPF main electrodes insulator made from PTFE  | 250 |
| Figure 6.26 DuPF Aluminum disc for earth   | 251 |
| Figure 6.27 DuPF main cathode collector grounded cylinder  | 252 |
| Figure 6.28 DuPF cathode grounded plugin tube  | 253 |
| Figure 6.29 DuPF stainless steel vacuum vessel   | 254 |
| Figure 6.30 DuPF stainless steel vacuum cylinder   | 255 |
| Figure 6.31 DuPF vacuum cylinder down flange   | 256 |
| Figure 6.32 DuPF vacuum cylinder upper flange  | 257 |
| Figure 6.33 DuPF vacuum vessel gate  | 258 |
| Figure 6.34 DuPF vacuum vessel stainless steel window tube   | 259 |
| Figure 6.35 DuPF vacuum vessel feedthrough tube  | 260 |
| Figure 6.36 DuPF vacuum vessel stainless steel window flange   | 261 |
| Figure 6.37 DN10 vacuum flange   | 262 |
| Figure 6.38 DN25 flange  | 263 |
| Figure 6.39 DN40 vacuum flange   | 264 |
| Figure 6.40 DuPF vacuum vessel window glass  | 265 |
| Figure 6.41 DuPF vacuum vessel assembling  | 266 |



|  |     |
|--|-----|
| Figure 6.42 DuPF electrodes and vacuum vessel assembling                                   | 267 |
| Figure 6.43 DuPF main table made of stainless steel  | 267 |
| Figure 6.44 DuPF main table stainless steel base   | 268 |
| Figure 6.45 DuPF main table cone which is installed on its stainless steel base            | 269 |
| Figure 6.46 DuPF main table sheet  | 270 |
| Figure 6.47 DuPF main table stainless steel tube   | 271 |
| Figure 6.48 DuPF main table  | 272 |
| Figure 6.49 DuPF electrodes, vacuum vessel and main table assembly                         | 273 |
| Figure 6.50 DuPF gas panel   | 274 |
| Figure 6.51 DuPF main gas cylinder   | 275 |
| Figure 6.52 DuPF gas panel side flange   | 276 |
| Figure 6.53 DuPF gas panel main cylinder side flange                                       | 277 |
| Figure 6.54 DuPF gas panel minor cylinder  | 278 |
| Figure 6.55 DuPF gas panel minor cylinder side flange                                      | 279 |
| Figure 6.56 DuPF gas panel junction tube   | 280 |
| Figure 6.57 DuPF gas panel stand plate   | 281 |
| Figure 6.58 DuPF gas panel 3-D   | 282 |
| Figure 6.59 DuPF electrodes, vacuum vessel and gas panel assembly                          | 283 |
| Figure 6.60 DuPF spark gap set up  | 284 |
| Figure 6.61 DuPF spark gap cylinder  | 285 |
| Figure 6.62 DuPF spark gap high voltage semi-sphere  | 286 |
| Figure 6.63 DuPF spark gap triggering semi-sphere  | 287 |
| Figure 6.64 DuPF spark gap PTFE box  | 288 |
| Figure 6.65 DuPF spark gap gas inlet-outlet tube   | 289 |
| Figure 6.66 DuPF spark gap assembly  | 290 |
| Figure 6.67 DuPF electrodes, vacuum vessel, main table, gas panel and spark gap assembling | 290 |
| Figure 6.68 DuPF stainless steel sample holder   | 291 |
| Figure 6.69 DuPF sample holder part  | 292 |
| Figure 6.70 DuPF sample holder vacuum fixer  | 293 |
| Figure 6.71 DuPF sample holder disc  | 294 |

|  |     |
|--|-----|
| Figure 6.72 DuPF sample holder handle  | 295 |
| Figure 6.73 DuPF sample holder rod     | 296 |
| Figure 6.74 DuPF sample holder shutter | 297 |

## CHAPTER 1

### Introduction and Literature Review

The plasma focus is typically operated in a coaxial geometry with an intense pinch mode. The dynamics comprises an axial acceleration phase, followed by a radial phase consisting of a fast compression, a pinch and an explosive pinch disruption phase. During these two last phases intense radiations are emitted including x-rays and powerful axially directed beams of ions and electrons. The break-up of the pinch also launches axially propagating fast plasma streams. This intense pinch mode is the subject of many studies and much research documentation. The intense radiations and beams and plasma emissions have many applications including fusion neutron generation and more recently the fabrication and deposition of advanced materials and the testing of potential wall materials in fusion-relevant situations.

The DPF facility acts as a type of plasma accelerator [1, 2] that produces directed hot ( $T_{pl} \sim 1$  keV) fast ( $v_{pl} > 10^7$  cm/s) dense ( $n_{pl} \approx 10^{16}$  to  $10^{19}$  cm<sup>-3</sup>) plasma streams, high energy ion ( $E_i \approx 0.01$  to 100 MeV) and electron ( $E_e \approx 0.01$  to 1.0 MeV) beams in addition to soft ( $E_{hv} \sim 0.1$  to 10 keV) and hard ( $E_{hv} \sim 10$  to 1000 keV) X rays and fusion neutrons ( $E_n \sim 2.45$  and 14 MeV).

Dense Plasma Focus devices, compared with other thermonuclear devices, have a number of important applications [3, 2]:

- These devices provide an opportunity to expose different materials and objects to pulsed radiations of various types – ion, electron, plasma, X ray, neutron and shock wave of high-power flux density (up to  $10^{13}$  W/cm<sup>2</sup> for fast electrons,  $10^{12}$  W/cm<sup>2</sup> for fast ions, plasma streams and X ray photons and up to  $10^9$  n/cm<sup>2</sup> for neutrons) with pulse duration in the range  $10^{-9}$  to  $10^{-6}$  s. Thermal loads in these devices produced by the above-mentioned streams and a discharge current may reach magnitudes up to  $10^{10}$  MW/m<sup>2</sup> with the characteristic time of action up to about  $10^{-4}$  s.

- Because most types of radiation generated by DPF are of penetrating nature these devices can produce important volumetric effects (in contrast to lasers).
- They enable the experimenter to choose the specific distribution of pulsed energy between all the above-mentioned types of ionizing radiation – soft and hard X rays, neutrons, electron, ion and plasma beams. This is possible because energy flux density may be significantly different for each type of radiation depending on the mode of operation of the device.
- These streams in DPF devices can be separated in time due to different velocities of their (quasi-)particles.
- These beams in DPF devices can also be separated in space due to different angular distributions and by application of a magnetic field or by using their dissimilar Linear Energy Transfer (LET).

These intense and varied radiations give important opportunities for new and sometimes unusual applications in pulsed radiation physics and chemistry in general, and in different branches of material sciences (radiation material science, nanotechnologies, dynamic quality control of machines and mechanisms during their operation, neutron activation analysis, etc.) in particular.

The physics of interaction of high-power pulses of radiation generated in different fusion devices with materials is especially important for study of damage produced in elements of these installations including the discharge chamber of the DPF itself, but specifically the plasma-facing walls of thermonuclear fusion installations with inertial (laser, wire-array Z-pinches and heavy ion fusion) and magnetic (Tokamak and Stellarator) plasma confinements. In the latter case DPF devices can simulate radiation sources, which are typical for the stressed regimes of the reactor's operation (ELMs, VDEs, disruption instability, etc.).

More recently it has become apparent that for the purpose of materials deposition and fabrication of nano-materials, the intensity of the radiation and beams may need to be controlled. It has been suggested that it may even be beneficial for some situations to eliminate or greatly reduce charged particle beams; for example for the deposition of certain nano-materials, especially from the point of

view of spatial homogeneity. Thus the reduction of the intensity of the pinch or even the elimination of the pinch sub-phase may be of use for such situations [4].

In order to extend the usefulness of the plasma focus for applications, it is important to better understand the fundamental processes in hot plasmas, so as to be able to optimize a certain device for a specific application. The aim of this project is to collate known behavior of the Fast Focus Mode (FFM) and investigate the behavior of Slow Focus Mode (SFM) of dense plasma focus [4] and compare their properties with a view to improve performance for material science applications.

In existing plasma focus facilities it is the established practice to maximize the yield in the production of any desired radiation. This in almost all cases means adjusting the plasma focus for intense compression [5] in a selected gas; for example for fusion neutrons, Deuterium is selected; for SXR lithography, neon is selected [6], for micro-machining, argon or a Deuterium-argon or argon-krypton mixture [7]. On the other hand for good deposition conditions it may be necessary to reduce focus intensity; using the focusing not so much for its explosive emission of intense radiation but for its storage of plasma energy and a subsequent release of the stored energy into streaming plasma. Using Lee Model code it has been recently developed the first modeling tool for the computation of plasma ion beams and high-speed plasma streams from the plasma focus [8, 9]. One of the results shows that a low-voltage, high-energy plasma focus has big advantages as a source of fast ion beams and high-speed plasma streams. In addition its dynamics could also be slowed down and its high energy be used to produce a longer more uniform pulse for materials fabrication. The SFM may thus be most useful in producing fast plasma stream FPS for nano-materials Fabrication [10, 11].

As part of this research we will explore the use of a single plasma focus device with two interchangeable anodes to produce two contrasting modes for:

- I. Intense ion beam and streaming plasma pulses for damage studies of potential fusion reactor wall materials, particularly of plasma-facing walls.
- II. High power long duration uniform flow of plasma ions and streaming plasma pulses for synthesis of nano-materials

Before continuing with the Introduction and Literature Review we first specify our Problem Statement and Objectives as follows.

### **1.1 Problem Statement**

What is predicted by Lee Model Code for FFM and SFM states in INTI PF machine? What are the neutron time of flight measurements in INTI PF machine during FFM? Is there any correlation between Lee Model Code and ion time of flight measurements in INTI PF machine? What are the applications of FFM and SFM in INTI PF machine? What are the FFM and SFM results for high energy plasma focus device using Lee Model Code? Is it possible to design a 160 kJ DuPF for material applications?

### **1.2 Research Objectives**

The objectives of this project are to conduct numerical and experimental studies of FFM and SFM of INTI PF machine using Lee Code, then to conduct numerical experiments and parameter design of the 160 kJ Dual plasma focus and finally to produce the complete industrial detail design and drawing of the Dual plasma focus with interchangeable electrodes by SolidWorks Software. Subsidiary objectives are to improve diagnostic capabilities by designing and constructing a photomultiplier-plastic scintillator system for D-D fusion neutrons and Hard X-Ray TOF measurements and a Fast Faraday Cup for ion beam measurements.